

# Dust-driven wind as a model of Broad Absorption Line quasars

M. H. Naddaf<sup>1,2,\*,</sup>, M. L. Martinez-Aldama<sup>3,4</sup>, P. Marziani<sup>5</sup>, S. Panda<sup>6</sup><sup>\*\*</sup>, M. Sniegowska<sup>2,1</sup>, and B. Czerny<sup>1</sup>

<sup>1</sup> Center for Theoretical Physics, Polish Academy of Sciences, Lotnikow 32/46, 02-668 Warsaw, Poland

<sup>2</sup> Nicolaus Copernicus Astronomical Center, Polish Academy of Sciences, Bartycka 18, 00-716 Warsaw, Poland

<sup>3</sup> Instituto de Física y Astronomía, Facultad de Ciencias, Universidad de Valparaíso, Gran Bretaña 1111, Valparaíso, Chile

<sup>4</sup> Departamento de Astronomía, Universidad de Chile, Casilla 36D, Santiago, Chile

<sup>5</sup> INAF-Astronomical Observatory of Padova, Vicoletto dell'Osservatorio, 5, 35122 Padova PD, Italy

<sup>6</sup> Laboratório Nacional de Astrofísica - Rua dos Estados Unidos 154, Bairro das Nações, CEP 37504-364, Itajubá, MG, Brazil

December 19, 2022

## ABSTRACT

**Context.** We test a scenario claiming that the broad absorption line (BAL) phenomenon in quasars (QSOs) is not a temporary stage of their life. In this scenario, we see the BAL effect only if the line of sight is within a spatially limited and collimated massive outflow cone covering only a fraction of the sky from the point of view of the nucleus.

**Aims.** The aim is to understand the theoretical mechanism behind the massive outflow in BAL QSOs which is important for modelling the impact of quasars onto the star formation rate in the host galaxy, and, subsequently, onto the galaxy evolution.

**Methods.** We apply the specific theoretical model of dust-driven wind, basically being developed to explain the Broad Emission Lines. The model has considerable predictive power. The 2.5D version of failed radiatively accelerated dusty outflow (FRADO) model of Czerny & Hryniwicz gives rise to the formation of fast funnel-shaped outflow from the disk for a certain range of black hole masses, Eddington ratios and metallicities. We now interpret BAL QSO as sources viewed along the outflowing stream and we calculate the probabilities of seeing the BAL phenomenon as functions of these global parameters, and we compare these probabilities to those seen in the observational data. We include considerations on the presence/absence of obscuring torus.

**Results.** Comparing our theoretical results with observational data for a sample of QSOs consisting of two sub-populations of BAL and non-BAL QSOs we found that both in the model and in the data the BAL phenomenon mostly happens for sources with black hole masses larger than  $10^8 M_\odot$ , the effect get stronger with accretion rate, and also high metallicities are more likely in QSOs showing BAL features if the presence of torus is taken into account.

**Conclusions.** The consistency of the model with the data provides support for the interpretation of the BAL phenomenon as the result of the orientation of the source. It also supports the underlying theoretical model although more consistency checks should be done in the future.

**Key words.** Active Galaxies, Accretion Disk, Radiation Pressure, FRADO Model, Dust, Broad Line Region, Broad Absorption Lines, Quasars, Dusty Torus

## 1. Introduction

Broad Absorption Line Quasars (BAL QSOs) were discovered around half a century ago (Lynds 1967). The peculiar blue-shifted absorption features in their spectra show a clear signature of massive energetic outflows from the underlying source (see e.g., Weymann et al. 1991) with typical outflow velocities of around several up to tens of 1000 km/s, but reaching 0.2 c in the most extreme cases (e.g. Risaliti et al. 2005; Rodríguez Hidalgo & Rankine 2022).

The massive outflows from BAL sources and their relatively wide opening angle can play an important role in the feedback process in active galaxies and its consequences on the evolution of the central black hole and galactic bulge (see e.g., Di Matteo et al. 2005; Elvis 2006; Hopkins et al. 2009; Moe et al. 2009; Hamann et al. 2019).

Depending on the studied sample, the BAL phenomenon is present in around 5% to even 40% of the total quasar population (see e.g., Weymann et al. 1991; Tolea et al. 2002; Knigge et al. 2008; Allen et al. 2011; Shen et al. 2019).

Observationally, however, we cannot differentiate between the two basic scenarios describing the BAL quasar phenomenon:

(i) the BAL phenomenon is a short stage in the quasar life cycle and the outflow is spherically symmetric (e.g. Surdej & Swings 1981; Drew & Boksenberg 1984; Voit et al. 1993; Krolik & Voit 1998),

(ii) the BALs occur in all QSOs showing signatures of outflow but we see BAL only if our line of sight is within the outflow cone that is collimated and spatially limited, covering only a fraction of the sky from the point of view of the nucleus (Young et al. 1999; Elvis 2000, 2012).

Both scenarios predict that only a fraction of QSOs shows BAL features, and cannot be distinguished just on the basis of statistical grounds, although scenario (i) is not anymore favoured (Turnshek 1988, and the references therein).

In this study, we follow the second scenario but we use a theoretical framework which allows us to actually predict the outflow cone as a function of quasar parameters. This, confronted with available statistics can tell us if our physically motivated model is a viable explanation of the BAL phenomenon.

Scenario (ii) is usually formulated as an empirical picture. Elvis (2000, 2012) proposed a likely line-driven funnel-shaped

\* naddaf@cft.edu.pl

\*\* CNPq Fellow

outflow with an inclination of around 60 degrees with respect to the symmetry axis and an opening angle of 6 up to 12 degrees. The corresponding covering factor of the funnel which is between 0.1 to 0.2 is then assumed as the BAL prevalence or the probability of observing the BAL effect, equivalently referring to the 10 to 20% population of BAL QSOs to all quasars. The geometry is of course purely empirical without any physical parameters included to constrain the geometry of the outflow but it accounts for all emission and absorption features.

This picture, however, does not account for all BAL properties. The outflow in the picture of Elvis (2000) is assumed to be powered by a line-driving mechanism, while studies of BAL objects imply the presence of dust with a reddening curve characteristic of predominately large grains (see e.g. Dunn et al. 2010; Bautista et al. 2010), hence making dust-based models of the outflow crucial. Moreover, the range of distances for the location of outflow is reported to be much further away (see e.g., Korista et al. 2008; Dunn et al. 2010; Borguet et al. 2013; Chamberlain et al. 2015) than acceleration region of winds frequently obtained based on line-driving mechanism (Murray et al. 1995; Proga & Kallman 2004; Waters et al. 2021), thus favours the dust-driving scenario which works at radii larger by a factor  $\sim 10$ .

In this paper, we thus aim at testing the theoretical model of dusty winds, basically being developed to explain the broad emission lines (Czerny & Hryniewicz 2011; Naddaf & Czerny 2022) against the observational data for BAL QSOs. The failed radiatively accelerated dusty outflow model, known as FRADO, works at the basis of a dust-driving mechanism in which disk radiation pressure acting on dust lifts up the clumpy dusty material, initially in Keplerian orbits around the central black hole, from the disk surface. Once lifted, the material may either follow a closed loop and fall back onto the disk surface or may gain high velocities enough to escape the gravitational potential of the central black hole towards the torus. The material depending on the trajectory may either lose the dust content due to being irradiated by intense central disk radiation if reaching high altitudes or remain dusty for the full time of flight.

The dust-driving mechanism, therefore, gives rise to the formation of the funnel-shaped stream of material (Naddaf et al. 2021) consistent with the empirical model of Elvis (2000). However, the model gives specific predictions for the outflow geometry, depending on the black hole mass, Eddington ratio and the metallicity of the disk material. As in the previous approach, we expect the BAL phenomenon if the viewing angle towards the nucleus is within the outflow cone. We aim to see if the theoretically predicted trends with quasar parameters are consistent with observations of BAL QSOs.

Therefore the paper is structured as follows. We introduce the sample of BAL QSOs we selected for the purpose of this study in Section 2. The theoretical model of dusty winds describing the geometry of massive outflow along with the grid of simulations is introduced in Section 3. The results are presented in Section 4, followed by discussion in Section 5.

In the following, we use the definitions of the basic parameters for a single source as

$$M_\bullet = M_{\text{BH}}/M_\odot, \quad \dot{m} = \dot{M}/\dot{M}_{\text{Edd}}, \quad \alpha_{\text{Edd}} = L/L_{\text{Edd}},$$

where  $M_\bullet$  is the dimensionless mass of the black hole in solar units, and  $\dot{m}$  and  $\alpha_{\text{Edd}}$  are the dimensionless accretion rate and luminosity of the source in Eddington units, respectively.

## 2. Selected BAL QSOs observational sample

For the current study, we use the quasar catalogue of the Sloan Digital Sky Survey DR7 (Shen et al. 2011). This catalogue provides an identification of the CIV  $\lambda 1549$  High and MgII  $\lambda 2800$  Low BALQSO, respectively. We performed a visual inspection to ensure the correct identification of the BAL systems. The objects were classified according to their spectral appearance in high BALQSO (HB) showing only the absorption transitions from highly ionized atoms, low BALQSO (LB) showing both the high-ionization transitions and absorption lines from lower-ionization ions in their rest-UV spectra, miniBALQSO (MB) and FeLow BALQSO (FLB) that shows FeII absorption lines. An example of each spectral type is shown in Fig. 1.

MB objects were excluded because they are characterized by systematically narrower troughs, often associated with blended narrow line absorptions, and their Balnicity index is 0 (Weymann et al. 1991). The MB phenomenology suggests that they belong to a physical scenario different from the one of LB and HB (Vestergaard 2003; Sulentic et al. 2006). FLB is thought to represent an extreme aspect of the BAL phenomenon (Choi et al. 2022b,a); however, due to the complex appearance of their spectra, strongly affected by deep and broad FeII absorptions all

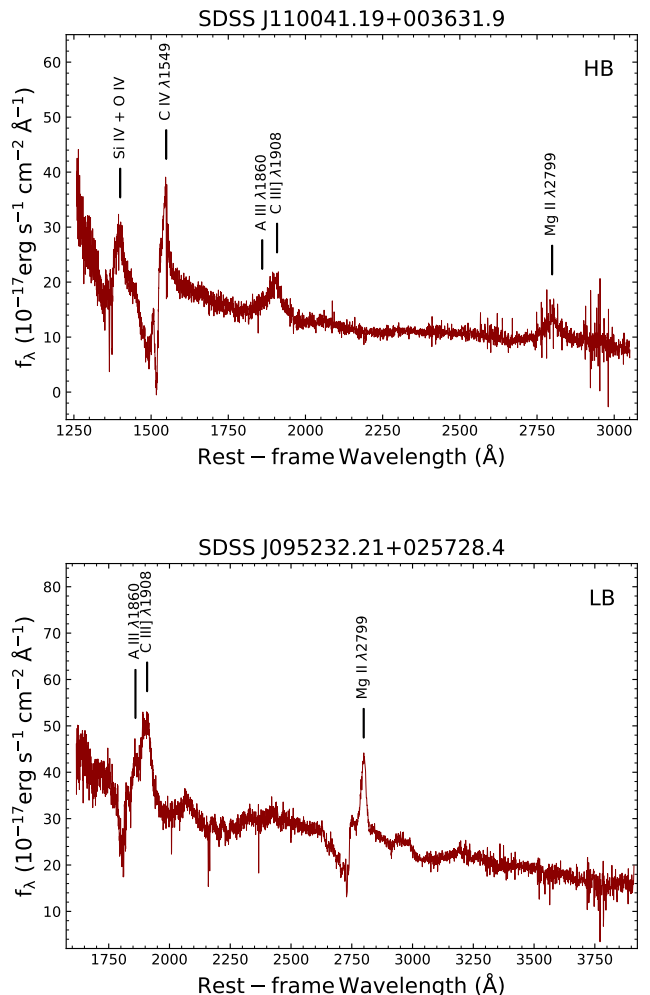


**Fig. 1.** Representative SDSS spectrum for a high BALQSO (upper panel) and a low BALQSO (lower panel) from our working sample. The spectra have been scaled to rest-frame wavelengths. The prominent emission lines are marked on the spectra.

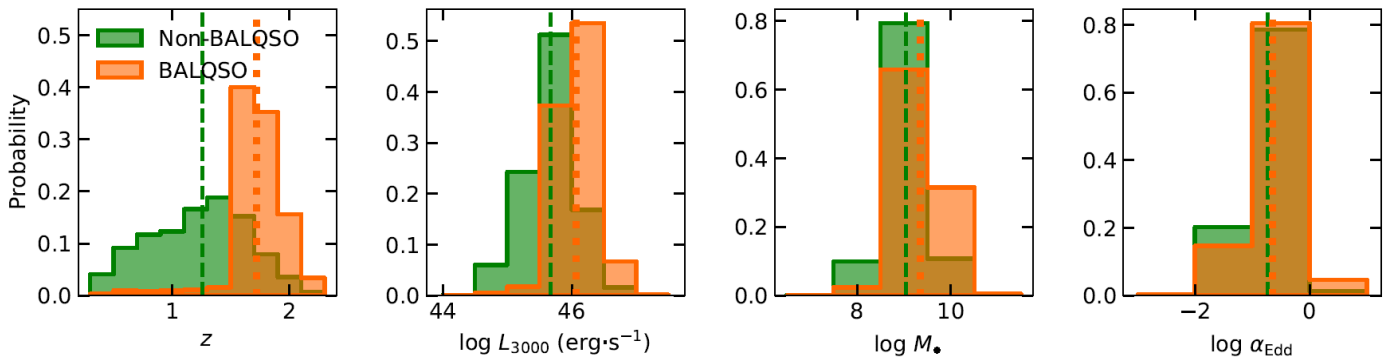


**Fig. 2.** Redshift ( $z$ ), luminosity at 3000Å ( $L_{3000}$ ), black hole mass ( $M_{\bullet}$ ) and Eddington ratio ( $\alpha_{\text{Edd}}$ ) distributions for the non-BALQSO (red,) and BALQSO (green) samples selected from [Shen et al. \(2011\)](#) catalogue. Vertical dashed and dotted lines indicate the median values for non-BALQSO and BALQSO, respectively.

across the UV range, relevant physical parameters and even redshifts are poorly known. The FLBs identified for the present work are a small subsample, and are excluded from the analysis of the present work, as dedicated work is needed to properly ascertain their properties. This goes beyond the scope of the present analysis.

A full sample of sources with median  $S/N > 10$  per pixel in the rest-frame 2700-2900Å region MgII ([Shen et al. 2011](#), Tab. 1 Col. 102) and with black hole masses estimated from MgII  $\lambda 2800$ . The latter condition is necessary because in the UV range this emission line is a better virial estimator than CIV  $\lambda 1549$  (e.g. [Mejía-Restrepo et al. 2016](#)). The full sample includes 42,349 objects where 40,991 and 1,358 are non-BALQSO and BALQSO (HB and LB), respectively. The MgII black hole mass and the Eddington ratio were taken from the SDSS catalogue ([Shen et al. 2011](#), Tab. 1 Col. 135 and Col. 141, respectively).

Summarizing up, the sample spans a redshift, luminosity at 3000Å, black hole mass and Eddington ratio ranges of  $0.3501 < z < 2.2487$ ,  $45.04 < \log L_{3000} < 48.19$ ,  $7.28 < \log M_{\bullet, \text{MgII}} < 11.31$ , and  $-2.88 < \log \alpha_{\text{Edd}} < 0.69$ , respectively. Fig. 2 shows the distributions of  $z$ ,  $\log L_{3000}$ ,  $\log M_{\bullet}$ , and  $\log \alpha_{\text{Edd}}$  for the BALQSO and non-BALQSO samples. The Eddington ratio for BAL and non-BAL samples seem similar, but the masses in BAL quasars are on average higher, and (consistently) luminosities are on average higher. BAL quasars seem to be located systematically at higher redshifts, which might also reflect the fact that statistically, we detect higher mass quasars at higher redshifts (e.g. [Vestergaard & Peterson 2006](#)). According to  $p$ -values ( $\ll 0.01$ ) of a Kolmogorov-Smirnov (KS) two-sided test, all the distributions are drawn from different parent populations.

### 3. Theoretical model

The 2.5D FRADO model ([Naddaf et al. 2021](#)) which is a relatively simple non-hydrodynamical approach to the dynamics of low ionized part of BLR leads to the formation of a fast outflow from the disk for a large black hole masses, Eddington ratios and metallicities, although it is based on radiatively dusty-driving mechanism and addresses the farther part of BLR located at around a few thousand  $r_g$  where the disk is cold enough for the dust to form. The basic FRADO model ([Czerny & Hryniwicz 2011; Czerny et al. 2015, 2017](#)) describing the dynamics of BLR material in one dimension, i.e. vertical with respect to the disk plane, could not address the outflow feature, but the 2.5D enhanced version of model ([Naddaf et al. 2021](#)) predicted the

emergence of such a feature, for a certain range of the source global parameters.

The predictions of the 2.5D version of dust-driven outflow from the accretion disk were recently tested against the observational data with the radius-luminosity relation ([Naddaf et al. 2020](#)) and the shape of observed broad emission lines in quasars ([Naddaf & Czerny 2022](#)), which altogether make the model an interesting case for further studies. Therefore, we intend in this work to investigate the geometry of the outflow originating from the accretion disk in the low-ionized part of BLR based on the 2.5D FRADO model.

#### 3.1. Dust-driving mechanism in 2.5D FRADO

The basic FRADO model analytically described only the failed dusty wind motion and only in a 1D approximation (vertical motion with respect to the disk plane), folding the radiation flux of the accretion disk with the wavelength-averaged dust opacity ([Czerny & Hryniwicz 2011; Czerny et al. 2015, 2016, 2017](#)). Despite many interesting results in explaining the geometry and physics of broad line region, it was not able to catch the dynamical picture of a likely expected outflowing wind.

In 2.5D FRADO, the clumpy dusty material, initially in Keplerian orbits around the central black hole, is launched due to radiation emitted by the whole extended disk acting on dust at the disk surface. Radiation is geometrically moderated by the shielding which depends on the cloud location (see [Naddaf et al. 2021](#), for details). Known as *shielding effect*, it is a requirement, protecting the early lifted clumps from too early sublimation by the intense central disk radiation, necessary to launch an efficient outflow (see e.g., [Murray et al. 1995; Risaliti & Elvis 2010; Naddaf et al. 2021](#)). The radiation pressure force is calculated allowing for wavelength-dependent dust opacities for a range of dust grains as in [Röllig et al. \(2013\)](#), and the assumed dust distribution comes from [Mathis et al. \(1977\)](#). The radiative force is thus calculated by convolving the locally available radiation flux, including its spectral shape, with the wavelength-dependent cross-section for dust scattering and absorption (for more details, see [Naddaf et al. 2021](#)).

In 2.5D FRADO, the full pattern of the trajectories of clumpy dusty-gaseous material launched at different radii of the disk is complex and depends on the main global parameters of the source, such as mass, Eddington rate and metallicity. They determine the launching radius, and if the available radiative force is not strong enough, the lifted material later returns to the disk surface, hence forming a failed wind. If the available radiative

force is high enough the material will escape toward the torus in the form of a fast outflowing stream of material. The dust sublimation temperature is fixed at 1500 K for all dust grains (Baskin & Laor 2018; Gravity Collaboration et al. 2020), which consequently sets a geometrical location above the accretion disk, so-called *sublimation location* as depicted with a dark-red solid curved line in Figure 3, where the material crossing it up loses the dust content, otherwise remains dusty. The geometry of the low-ionized part of BLR, including the outflowing wind, in the 2.5D FRADO model, is thus determined by the kinematics of the clouds, which in turn is set by global source parameters. For more details, we refer to our previous papers (Naddaf et al. 2021; Naddaf & Czerny 2022).

It should be also here noted that general relativistic effects are negligible at large radii appropriate for low-ionized BLR, so they are currently neglected in the model.

### 3.2. Outflow geometry and probability of BAL effect

When the source parameters allow launching the escaping wind, a geometrically funnel-shaped structure appears, as sketched in Figure 3. The radial range from which the launched material contributes to funnel formation is called *escaping zone*.

In order to determine the probability of the BAL effect in a single source we calculate the 3D trajectories of the material, and we determine whether for the adopted global parameters we identify the escaping zone. If so, we determine the minimum and the maximum of the viewing angle for the escaping trajectories, and we calculate the corresponding solid angle with respect to the nucleus. The ratio of this solid angle to the half of the sphere measures the probability of observing the BAL effect in the source. Likewise, if the presence of the torus is taken into account, we find the partial solid angle of the outflow not obscured by the torus and divide it by the part of the semi-sphere not subtended the torus. The probability of observing BAL is then given as

$$\Omega_{\theta_t} = \frac{\cos [\min(\theta_1 | \theta_t)] - \cos [\min(\theta_2 | \theta_t)]}{1 - \cos \theta_t} \quad (1)$$

where  $\theta_1$  and  $\theta_2$  are the minimum and maximum viewing angles of the outflowing funnel, and  $\theta_t$  is the opening angle of the torus, all angles with respect to the azimuthal axis.

The solid angle of the funnel of outflow strongly depends on all the source global parameters, i.e. black hole mass, Eddington ratio, and metallicity. It is merely determined on the basis of dust launching, and although eventual further acceleration of the launched material by line-driving will clearly change the velocities, it should not strongly affect the direction of motion. Therefore, our model should well represent the geometrical aspect.

### 3.3. Grid of models

We perform computations of the probability of the BAL phenomenon for a three-dimensional grid of parameters. Black hole mass,  $M_\bullet$ , was assumed to be between 6 and 10, on a logarithmic scale with a step size of one. For the dimensionless accretion rate,  $\dot{m}$ , we used four values: -2, -1, 0, and 1, also in the logarithmic scale. Finally, we considered values of the metallicity in the linear scale: 1, 2.5, 5 and 10, in solar units.

The range of masses for the central black hole and range of accretion rates are adopted as such in order to cover not only the domain of BAL QSOs available in the sample but also the

reasonable entire range of observed QSOs and even lower mass AGN. We did not consider lower accretion rates since then the flow towards the black hole may not always continue in the form of geometrically thin, optically thick disk (for a book on AGN properties, see Krolik 1999). We considered only solar and super-solar metallicities since most studies imply such a metallicity range (e.g. Juarez et al. 2009; Śniegowska et al. 2021; Garncica et al. 2022).

For each model, we calculate the trajectories for a very dense set of initial launching radii in order to have a high-resolution picture of the outflow geometry, if it forms, and we then determine the outflow cone parameters.

As for the presence of torus, the computation results are subject to further process with considered torus opening angles of 45, 60, 75, and 90 (no torus) degrees. These values are selected in such a way as to include the considered extreme modes of obscuration by a torus, and also two cases of mild obscuration.

Notably, the dust sublimation temperature is, kept at 1500 K in all cases, but the overall picture of the outflow geometry including the opening angle and orientation is not expected to be affected significantly, although the location of escaping zone is then shifted accordingly.

## 4. Results

### 4.1. Model predictions

We first calculated the grid of theoretical models, as outlined in Section 3.3. For each model, the dense grid of trajectories was calculated which allowed for precise determination of the geometry. An example is shown in the 2D projected perspective

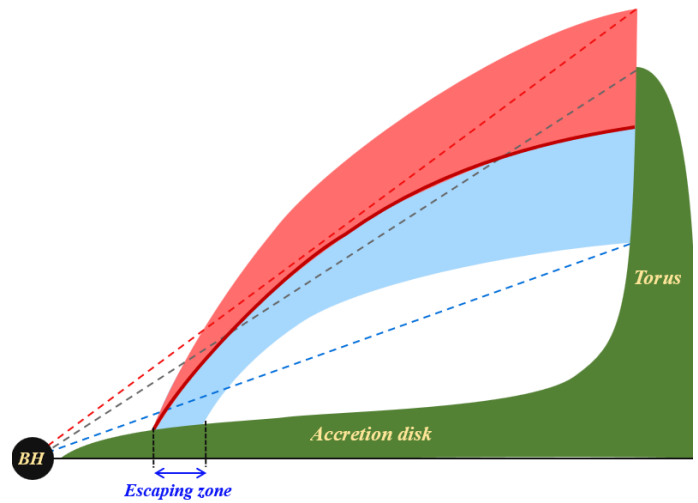


**Fig. 3.** The schematic 2D-projected illustration of massive outflow from the accretion disk due to the radiatively dust-driving mechanism. The *Radial extension of LIL BLR* is the entire radial range from which the material can be lifted from the disk surface; and the *escaping zone* represents the radial range from which all lifted material escapes to torus/infinity. The dashed lines indicate the reference angles with respect to the azimuthal symmetry axis, i.e. opening angle of the torus ( $\theta_t$ ), the minimum angle ( $\theta_1$ ) and maximum angle ( $\theta_2$ ) of outflow funnel (cone) which are shown in grey, blue, and red, respectively. The solid curved line in dark red represents the sublimation location where the material crossing it up loses the dust content. The regions in the funnel-shaped wind structure shaded in blue and red correspond to dusty and dustless material escaping, respectively.

in Figure 4. We see their many trajectories of dusty (blue) and dustless (red) material forming a failed wind, i.e. returning back to the disk although landing at a larger radius than the launch radius. However, for the present paper, those escaping are of key interest, marked with light blue and red belts, which form a thick funnel-shaped outflow. The light blue part remains dusty while in the red part dust was evaporated and the clouds there perform just a ballistic motion but they were already accelerated beyond the escape velocity. Line-driving mechanism may increase the opening angle of the outflow and boost the terminal velocities, but it is not yet incorporated into the model, so only the dust-driving mechanism does the job. Since for the parameters adopted in Figure 4 the escaping stream forms, we store its parameters in Table 1.

The first three columns of Table 1 from left to right shows the accretion rate of the disk, the mass of the central black hole, and the metallicity of the disk, respectively. The fourth and fifth column represents the minimum and maximum viewing angles of the outflow measured with respect to the symmetry axis, respectively. The last column shows the probability of observing BAL effect based on the Equation 1 without considering the presence of obscuring torus, i.e.  $\theta_t$  is set at 90 degrees, hence named as  $\Omega_{\text{full}}$ .

As shown in Table 1, the maximum viewing angles of the outflow in all cases tend to be around 81 degrees with a spread of about 10 degrees, i.e.  $\theta_2 = 81 \pm 5$ . However, for the minimum viewing angles of the outflow,  $\theta_1$ , we have a broad set of values ranging from  $\sim 15$  degrees up to  $\sim 78$  degrees, depending on the main global parameters of the source. The opening angle of the outflow can be therefore as low as a few degrees up to  $\sim 70$

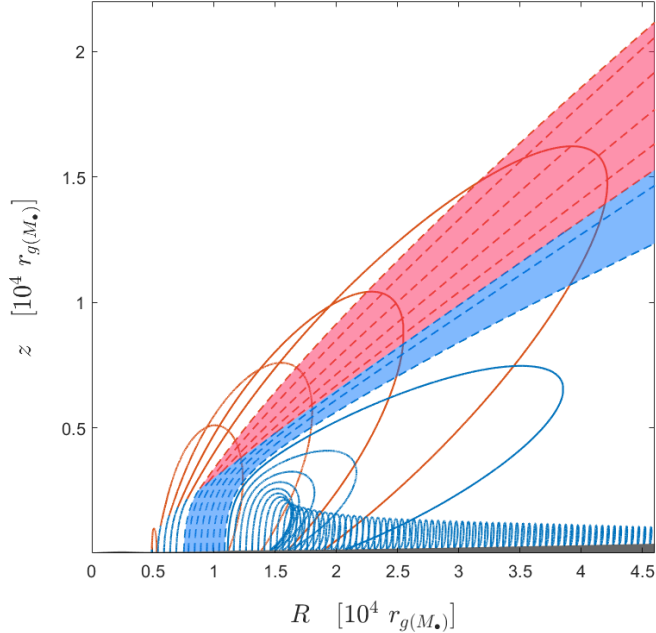


**Fig. 4.** An example of the trajectories of clouds above the accretion disk for the case of  $\log \dot{m} = 0$ ,  $\log M_\bullet = 8$ , and  $Z = 5Z_\odot$ . The motion is displayed in 2D plane of  $(R, z)$  in cylindrical coordinates due to azimuthal symmetry, where  $R$  is the radial distance to the black hole in the equatorial plane, and  $z$  is the vertical distance from the equatorial plane. The overall motion consists of failed wind (solid curved lines) and outflow (dashed lines) lines. Dusty and dustless situations are colour-coded in blue and red, respectively. Only a fraction of trajectories is shown for the matter of better visibility.

degrees. It is visible that with an increase in black hole mass, accretion rate, and metallicity, the values of  $\theta_1$  decrease, yielding a wider opening angle for the outflow.

**Table 1.** Geometrical properties of outflow

$\log \dot{m}$	$\log M_\bullet$	$Z/Z_\odot$	$\theta_1$	$\theta_2$	$\Omega_{\text{full}}$
1	8	1	69.68	79.13	0.1587
		2.5	55.96	80.12	0.3882
		5	46.70	79.94	0.5111
		10	25.34	81.31	0.7527
9	1	54.61	78.93	0.3871	
		2.5	35.76	79.85	0.6352
		5	23.95	83.12	0.7941
		10	19.73	85.99	0.8714
10	1	50.96	78.97	0.4385	
		2.5	21.66	81.83	0.7873
		5	18.35	84.12	0.8467
		10	15.48	85.78	0.8901
0	6	5	73.67	80.02	0.1079
		10	71.39	79.67	0.1398
7	2.5	72.96	80.02	0.1197	
		5	71.28	79.60	0.1404
		10	67.40	79.15	0.1961
8	1	75.48	79.93	0.0759	
		2.5	71.16	79.55	0.1415
		5	66.66	79.06	0.2064
		10	54.41	78.55	0.3835
9	1	71.40	79.65	0.1393	
		2.5	68.51	78.83	0.1726
		5	57.08	77.30	0.3236
		10	46.89	78.11	0.4774
10	1	67.75	78.72	0.1830	
		2.5	56.10	78.17	0.3527
		5	45.89	76.17	0.4570
		10	37.63	76.80	0.5636
-1	7	10	75.16	79.87	0.0802
		8	74.08	80.32	0.1061
		10	71.50	79.28	0.1313
9	2.5	75.29	80.21	0.0839	
		5	71.33	78.08	0.1136
		10	66.32	78.99	0.2106
10	1	77.61	78.69	0.0184	
		2.5	71.84	78.58	0.1137
		5	66.98	78.65	0.1943
		10	58.88	78.17	0.3118
-2	9	10	77.06	80.39	0.0570
		10	76.82	78.09	0.0216
		10	71.57	79.26	0.1298

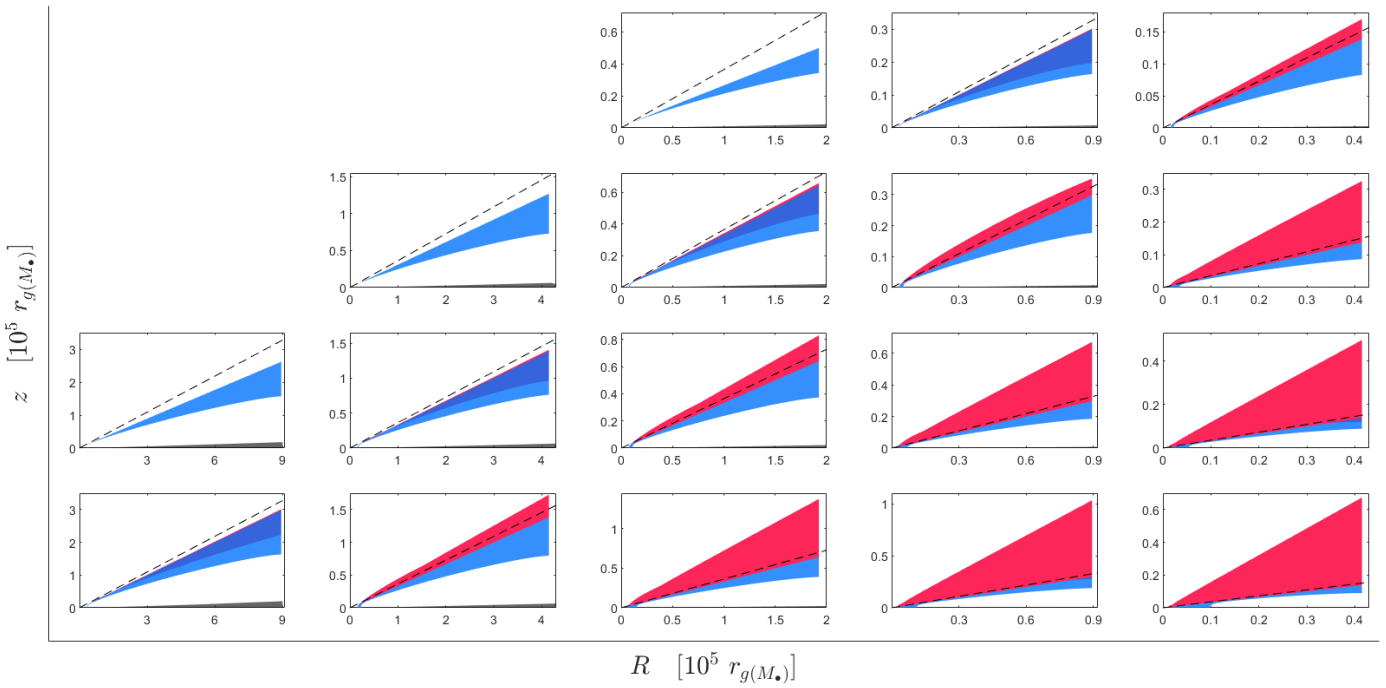


**Fig. 5.** The results of simulations showing the massive outflow triggered by disk radiation pressure for  $\dot{m} = 1$ . The  $M_\bullet$  is set at 6, 7, 8, 9, and 10 (in log units), from left to right, respectively. The adopted metallicities are 1, 2.5, 5, and  $10 Z_\odot$ , from top to bottom, respectively. The failed wind is not shown for better contrast. The accretion disk is shown as shaded grey area. Dusty and dustless components of the outflow funnel are shaded in blue and red, respectively. The black dashed line represents the arbitrary obscuration angle of 70 degrees by the torus, as a reference.

We show more examples (in fewer details, i.e. without failed wind) in Figure 5, for the Eddington accretion rate. Here we can see clearly the trend with the black hole mass and the metallicity. Both affect the outflow very strongly. Higher metallicity means more dust content and higher radiation pressure so the trend is rather natural. Also, a higher Eddington rate works in the same direction, enhancing the radiation force. We also observe a clear trend with the black hole mass. The change of the outflow with the source parameters is extremely important in our model: for low (solar) metallicity escaping zone forms only for larger black hole masses, and at high metallicity, the escape cone is much broader.

All results are stored in Table 1. The absence of the line in this table for some black hole masses, metallicities or Eddington rates means that there is no escaping zone formed for those parameters.

#### 4.2. Analysis of the observational sample

In order to compare the observational properties of BAL QSOs in our sample, we organize the results in two-dimensional space, parameterized by the source black hole mass and its Eddington rate for the  $\text{MgII} \lambda 2800$  emission line (see Fig. 6). The total number of non-BAL QSO with MgII mass measurements is large, 40 991 objects, and the number of BAL QSO is 1358, high enough to study some trends. The black hole mass values,  $\log M_\bullet$ , are predominantly located between 8 and 10, with the median values for non-BALQSO close to  $\log M_\bullet = 9.04$ , and for BALQSO close to  $\log M_\bullet = 9.34$ , a factor of 2 higher. We thus see there is already a trend of the rising probability of BAL phenomenon with the black hole mass, which is statistically significant according to the KS test (see Sec. 2).

In order to compare the observational results with the theoretical models, the two-dimensional space occupied by the sam-

ple  $M_\bullet$ - $\alpha_{\text{Edd}}$  is divided into bins centered at  $\Delta \log M_\bullet = [7.0, 8.0, 9.0, 10.0]$  and  $\Delta \log \alpha_{\text{Edd}} = [-2.0, -1.0, 0.0]$ . Figure 6 shows the division of the  $M_\bullet$ - $\alpha_{\text{Edd}}$  space indicating the number of sources, redshift, luminosity at  $3000\text{\AA}$ , black hole mass, and Eddington ratio for non-BALQSO (left panel) and BALQSO (right panel) in each bin. Applying a KS test for redshift, luminosity, black hole mass and Eddington ratio in each bin, we found  $p$ -values smaller than 0.01, which indicates a different parent distribution, such as the case of the full sample. In order to get a statistical consistency in each bin, we applied a bootstrap resampling, (see Sec. 4.3).

Contour lines show the object density distribution, and overall BAL QSO distributions are not only shifted towards higher black hole masses but are also more extended towards higher Eddington ratios, although the median for the Eddington rate is not much different. The distribution of BAL QSO seems to be also more inclined with respect to the axis, i.e. towards higher mass lower Eddington ratio and lower mass higher Eddington ratio. When specific sub-types of BAL QSO are analyzed, the distribution in two-dimensional space seems always more extended.

#### 4.3. Bootstrap resampling

Table 2 provides the observed prevalence of the BAL QSOs within intervals of black hole mass and Eddington ratio. We observe a trend in the sample that BAL QSO seems to have a larger mass than non-BAL objects.

In order to assess the statistical significance of this trend, we perform a bootstrap analysis. Within each bin, a bootstrap resampling was carried out in bins where the number of non-BAL and BALQSO sources is higher than 10. One thousand simulated samples were computed, with the condition that the distributions of the  $M_\bullet$  and  $\alpha_{\text{Edd}}$  do not differ significantly at a  $2\sigma$  confidence level, and that any systematic difference between

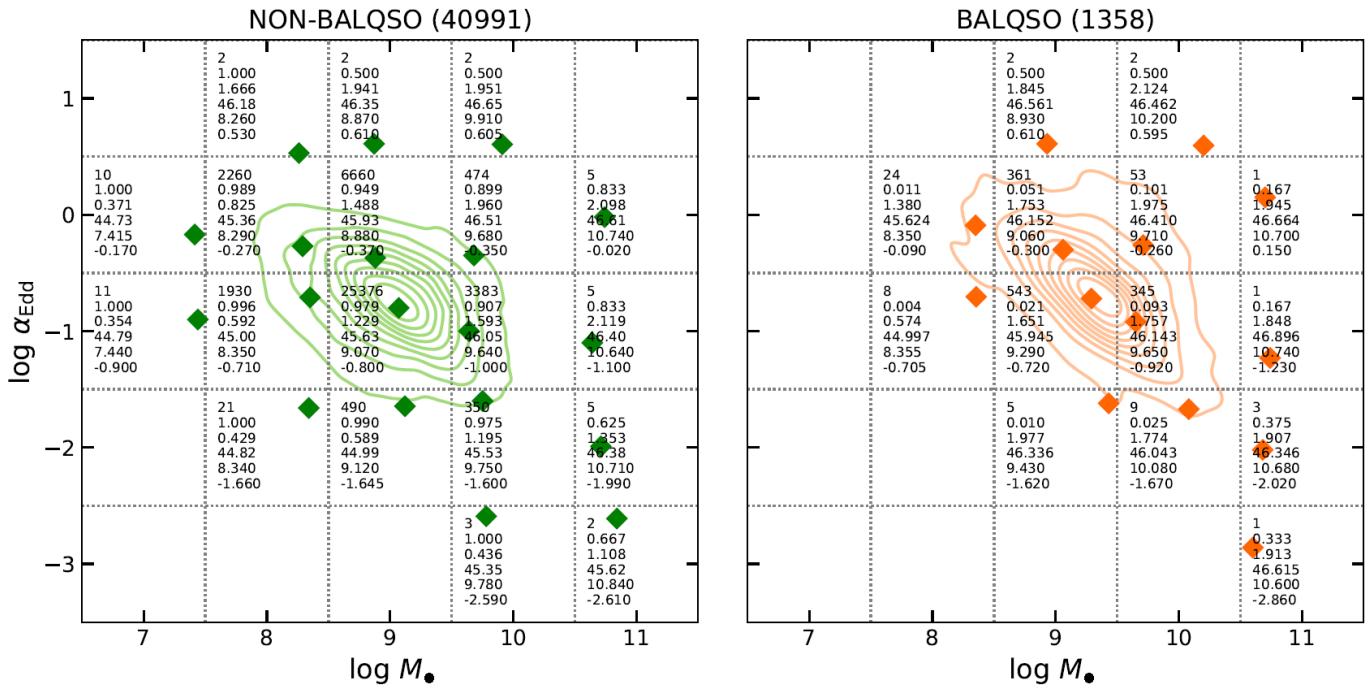


**Fig. 6.** Black hole mass and Eddington ratio space for non-BALQSO (left panel) and BALQSO (right panel). The space is divided into bins centered at  $\Delta \log M_\bullet = [7.0, 8.0, 9.0, 10.0]$  and  $\Delta \log \alpha_{\text{Edd}} = [-2.0, -1.0, 0.0]$ . Contours correspond to the full sample for each case, while diamond symbols correspond to the median values of  $\log M_\bullet$  and  $\log \alpha_{\text{Edd}}$  in each bin. The number of sources, the ratio of non-BALQSO (or BALQSO) with respect to the total sample size, and the median values of redshift,  $\log L_{3000}$ ,  $\log M_\bullet$ , and  $\log \alpha_{\text{Edd}}$  are listed in each bin.

the median of the  $M_\bullet$  and  $\alpha_{\text{Edd}}$  distribution is less than 0.1 dex. This was achieved by modelling the  $M_\bullet$  and  $\alpha_{\text{Edd}}$  distributions of the non-BAL sources on the distribution of the BAL QSOs, and accounted for any remaining bias in the distributions of the non-BAL QSOs and BAL QSOs. The effect is quite significant if biases are strong, for example in the case of the  $8.5 - 9.5 M_\bullet$  range, and  $-1.5$  to  $-0.5 \alpha_{\text{Edd}}$  range. Figure 7 shows that there is a significant increase in the BAL prevalence as a function of  $M_\bullet$ : from the lowest bin centred at  $\log M_\bullet \sim 8$  to the highest mass bin at  $\log M_\bullet \sim 10$  there is more than a 5-fold increment for  $-0.5 < \log \alpha_{\text{Edd}} < 0.5$ ; the increase is more than 10-fold for  $-1.55 < \log \alpha_{\text{Edd}} < -0.5$ . Separating the BAL prevalence in two broad Eddington ratio ranges,  $-1.5$  to  $-0.5$ , and  $-0.5$  to  $+0.5$ , is not suggesting any significant change in the prevalence as a function of  $\alpha_{\text{Edd}}$ . As a matter of fact, there is a strong trend of the BAL prevalence as a function of  $\alpha_{\text{Edd}}$ : Figure 8 showing that for all the three mass ranges there is a strong increase as a function of  $\alpha_{\text{Edd}}$ , reaching a maximum value  $\approx 0.45$  for the highest masses and for the highest  $\alpha_{\text{Edd}}$  in correspondence of the Eddington limit (right panel of Fig. 2). In the distributions of Figure 7 the difference is washed away because of the small number of sources radiating close to the Eddington limit: for the range centred at  $\log M_\bullet \sim 10$ , they are just 5% of all QSOs (19 out 407). The increase is well-described by an exponential function, as detailed in Section 4.4.1.

#### 4.4. Simulations confronted against observational data

##### 4.4.1. Without torus

The observational data for BAL prevalence ratio along with simulation results of the BAL effect probability for the torus-absent cases ( $\Omega_{\text{full}}$ , opening angle of 90 degrees) is shown in Figure 9, overplotted with the best exponential fit in each case. The results

in Figure 9 are colour-coded in black for the observational data, and blue, red, magenta, and green for the simulation output with metallicities of 1, 2.5, 5, and 10, respectively. In all cases, the confidence intervals of  $1-\sigma$  are shown as shaded belts embedding the best fit.

We see that in general, the quantitative predictions of the FRADO model overlap with the data in the entire mass range. We see that for low accretion rates the solar metallicity is favoured, and for the Eddington rate, higher metallicities give better consistency with the model. This is an expected trend, modelling of the broad emission lines in the optical plane also favours higher metallicity for a higher Eddington rate (Martínez-Aldama et al. 2018; Panda et al. 2018, 2019; Śniegowska et al. 2021; Garnica et al. 2022). We do not see a trend with the black hole mass: the requested rise in the metallicity takes place in all cases above  $\dot{m} \sim 3$ , i.e. only for super-Eddington sources, and this rise is not high, metallicities only up to 2 are required for  $\dot{m} = 3$ , although they rise steeply for still higher Eddington rates.

##### 4.4.2. With the presence of torus

If the torus is taken into account, the overall trend with the black hole mass remains the same, but the trend with metallicity is affected. To make an easier comparison, the residual of the best-fit exponential functions for computational results of the probability of observing BAL is subtracted by the exponential best-fit for the prevalence ratio based on observational data and is presented in Figure 10. The same colour code as in Figure 9 is followed for the Figure 10, i.e. the results for metallicities of 1, 2.5, 5, and 10 are represented in blue, red, magenta, and green, respectively.

For a thick torus (opening angle 45 deg), the results require the metallicity above 10 for the Eddington ratio crossed 1. For thinner, less shielding torus, the required metallicity is more

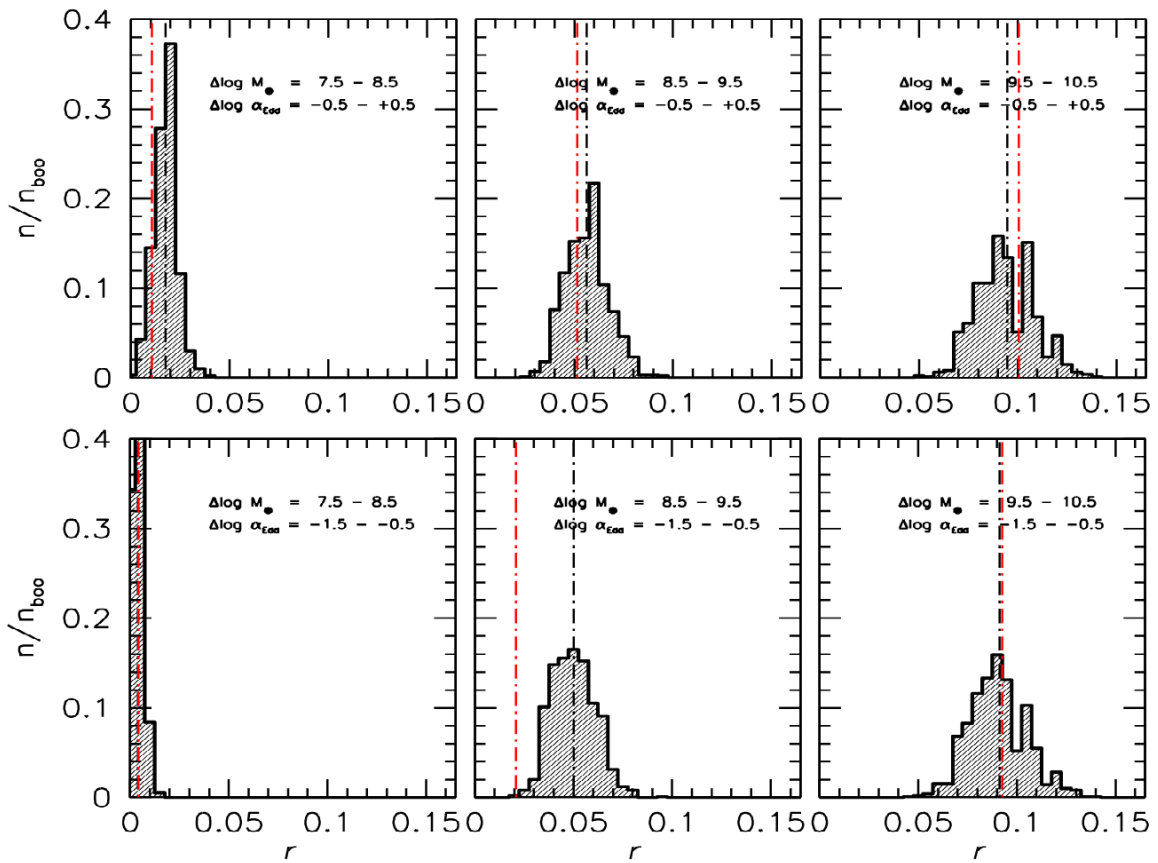


**Fig. 7.** Distributions of the ratio  $r = n_{\text{BAL}}/n_{\text{Total}}$  for 1000 bootstrap replications, in six ranges limited in  $M_{\bullet}$  and  $\alpha_{\text{Edd}}$ . The black dot-dashed line is the average of the bootstrapped distributions; the red one traces the original  $r$  value from each bin sample.

**Table 2.** Observed BAL QSO prevalences as determined directly from the sample (original), and the corresponding distribution properties obtained from bootstrap (resampled)

$\Delta \log \alpha_{\text{Edd}}$		-0.5 up to 0.5			-1.5 up to -0.5		
		$\Delta \log M_{\bullet}$	7.5 – 8.5	8.5 – 9.5	9.5 – 10.5	$\Delta \log M_{\bullet}$	7.5 – 8.5
Original	$n_{\text{nonBAL}}$	2260	6660	474	1945	25377	3383
	$n_{\text{BAL}}$	24	361	53	8	543	345
	$r$	0.011	0.051	0.101	0.004	0.021	0.093
	$\mu_{\frac{1}{2}}(\log M_{\bullet})_{\text{BAL}}$	8.36	9.06	9.71	8.38	9.29	9.65
	$\delta \log M_{\bullet}$	+0.07	+0.18	+0.03	+0.03	+0.22	+0.01
	$\mu_{\frac{1}{2}}(\log \alpha_{\text{Edd}})_{\text{BAL}}$	-0.07	-0.30	-0.26	-0.65	-0.72	-0.92
	$\delta \log \alpha_{\text{Edd}}$	+0.20	+0.07	+0.09	+0.03	+0.08	+0.08
Resampled	$r$	0.017	0.056	0.095	0.004	0.051	0.091
	$\sigma$	0.006	0.011	0.014	0.0026	0.010	0.014
	$\mu_{\frac{1}{2}}(\log M_{\bullet})_{\text{BAL}}$	8.263	9.085	9.762	8.250	9.414	9.701
	$\delta \log M_{\bullet}$	0.069	0.092	0.029	-0.052	0.027	0.022
	$\mu_{\frac{1}{2}}(\log \alpha_{\text{Edd}})_{\text{BAL}}$	0.088	-0.290	-0.155	-0.760	-0.832	-0.945
	$\delta \log \alpha_{\text{Edd}}$	0.103	0.050	0.043	-0.001	0.091	0.052

$r = n_{\text{BAL}}/n_{\text{Total}} = n_{\text{BAL}}/(n_{\text{BAL}} + n_{\text{nonBAL}})$ ,  $\mu_{\frac{1}{2}}$  corresponds to the median value in each case,  $\delta \log M_{\bullet}$  and  $\delta \log \alpha_{\text{Edd}}$  are defined as the median of BALs minus medians of non-BALs. Median values are shown in Fig. 7.

moderate. Observations support the presence of the shielding torus, its typical parameters are not firmly established but the values of the order of 60 - 80 deg for the opening angle measured from the symmetry axis are usually derived (Lawrence &

Elvis 2010; Alonso-Herrero et al. 2011; Guainazzi et al. 2016; Prince et al. 2022). This would push our results based on BAL modelling toward metallicities of the order of a few times the solar value.

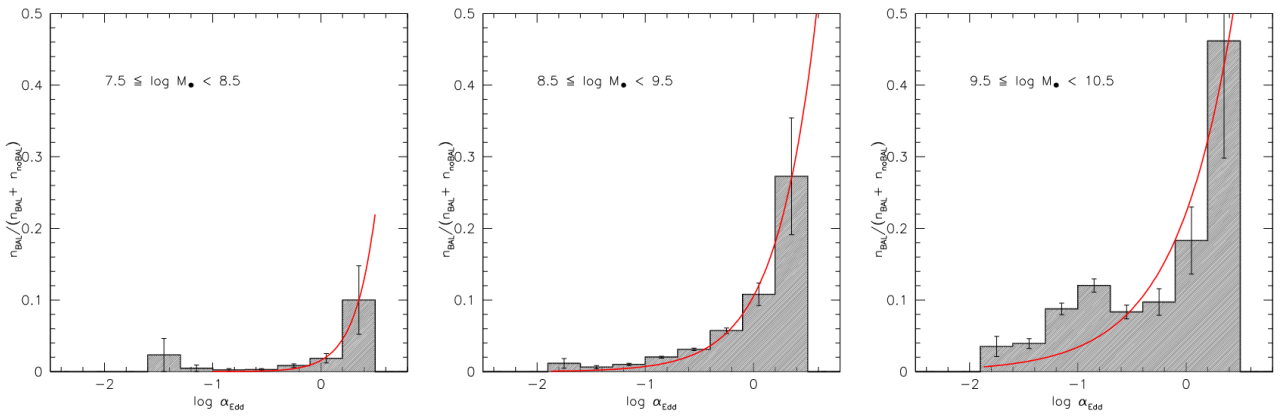


**Fig. 8.** Distributions of the prevalence ratio  $r = n_{\text{BAL}} / (n_{\text{BAL}} + n_{\text{noBAL}})$  as a function of Eddington ratio, for three  $M_{\bullet}$  ranges. Error bars have been computed following Poissonian statistics.

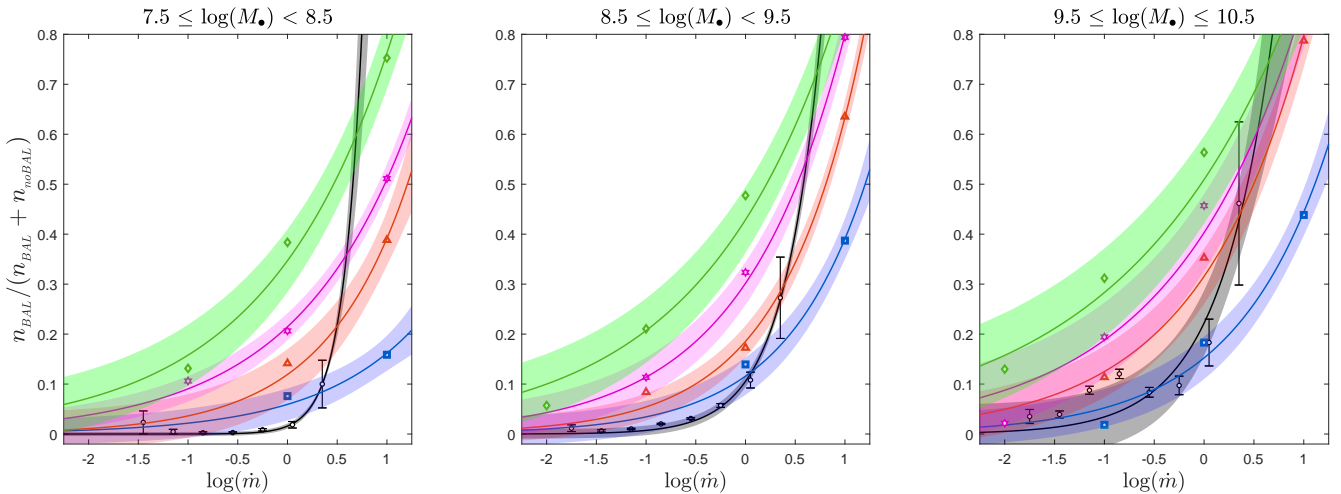


**Fig. 9.** Distributions of the prevalence ratio  $r = n_{\text{BAL}} / (n_{\text{BAL}} + n_{\text{noBAL}})$  as a function of Eddington ratio, for three  $M_{\bullet}$  ranges compared to simulation data for the case without torus. Observational data is displayed in black. Metallicities of 1, 2.5, 5, and 10 are depicted in blue, red, magenta, and green, respectively. Solid lines in each case show the best exponential fit to the corresponding data. Torus is not included here.

## 5. Discussion

We present the first results of the comparison of a theoretical model, FRADO, with the probability of observing the BAL phenomenon based on the solid angle covered by the dust-driven outflow. The results are encouraging. The model predicts no BAL effect in sources with low black mass. The outflow cone forms and gets wider with an increase in the black hole mass, Eddington rate and metallicity. The trends predicted by the model are supported by a sample of BAL and non-BAL QSOs from the SDSS DR7 Quasar catalogue (Shen et al. 2011).

### 5.1. Trends in the model and the data

In the model, all three global parameters: mass, Eddington rate and metallicity enhance the outflow and increase the fraction of the sky covered by the outflow from the point of view of the source, rising the probability to see the BAL phenomenon.

The selected subsample of non-BAL sources is large (40,991 objects), and the non-BAL sources are less numerous (1,358 sources) but enough to see some trends. The increase of the BAL probability with the black hole mass seems to be well visible. The trend with the Eddington ratio is also clear (see Figures 8 and 9), and if all parameters are combined we seem to see a need

for higher metallicity in higher Eddington sources if the sources should follow the model. Unfortunately, we do not have metallicity constraints for individual sources, only the mass and the Eddington ratio. However, such a trend - a rise of the metallicity with the Eddington rate - is frequently concluded in the independent studies (e.g. Martínez-Aldama et al. 2018; Panda et al. 2018, 2019; Śniegowska et al. 2021; Shin et al. 2021; Panda & Skorek 2022; Garnica et al. 2022), although some studies rather find a trend of metallicity ratio just with the black hole mass (e.g. Matsuoka et al. 2011).

We could not claim that the BAL phenomenon is not expected in low mass AGN ( $\log M_{\bullet} \sim 6 - 7 M_{\odot}$ ), the UV wavelength range is not covered in the SDSS DR7 observations, which does not permit the identification BAL sources in low mass AGN. However, using observation from the Hubble Space Telescope and International Ultraviolet Explorer observations, Sulentic et al. (2006) reported the identification of 12 BAL QSO at  $0.05 < z < 0.46$  with an average mass of  $\log M_{\bullet} \sim 8.1 M_{\odot}$ , which is similar to the minimum value given by the SDSS DR7 quasar sample. In order to clarify the presence of the low mass BAL QSO, good UV data, particularly in a sample of high Eddington ratio AGNs, is needed.

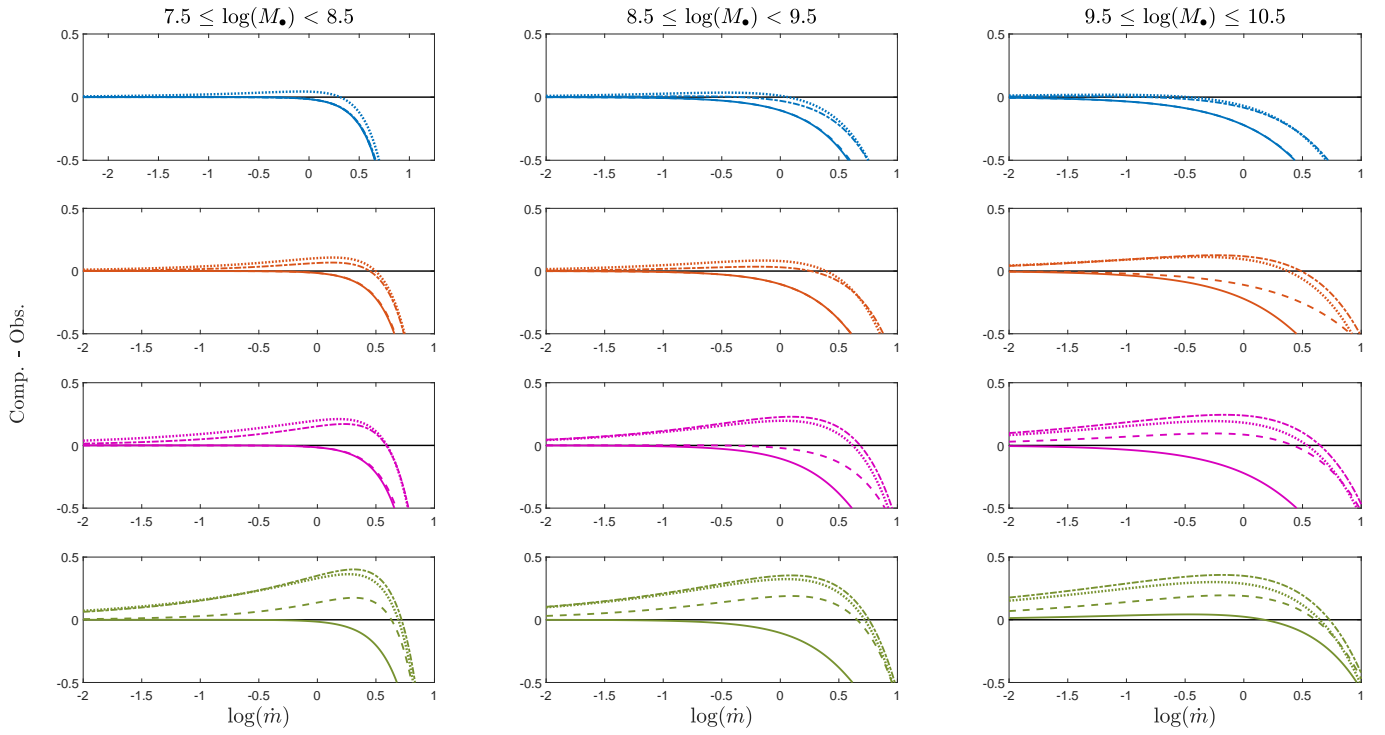


**Fig. 10.** Residual of the computational results of the probability of observing BAL (simulations) subtracted by prevalence ratio (observational data). Four adopted values of metallicities of 1, 2.5, 5, and 10 are represented in blue, red, magenta, and green colours. The black solid line is depicted as a reference for observational data. Solid, dashed, dash-dotted, and dotted lines correspond to opening angles of torus 45, 60, 75, and 90 (no torus), respectively. Results are presented as a function of Eddington ratio (in steps of 0.3 dex) for 3  $M_\bullet$  ranges.

## 5.2. Model assumptions

The FRADO model which allows us to calculate the opening angle of the outflowing stream is based on a number of assumptions. The model assumes the launch of the outflow is just due to radiation pressure acting on dust. We discuss the potential problem with this assumption below. The model is not a hydro, so cloud collisions, and actually cloud formation is not described, but the motion is highly supersonic so the effects of the pressure can be neglected. Later more advanced model can be built, but this is not straightforward due to the extended character of the disk powering the outflow and the need to include the dust evaporation role in the cloud dynamics.

### 5.2.1. Dust sublimation temperature

In the present work, the sublimation temperature of dust is set at 1500 K. Its precise value depends on the dust's chemical composition as well as the grain size (see [Baskin & Laor 2018](#); [Panda et al. 2020](#), and the references therein). Selective dust evaporation is too complex to include in the present dynamical model. Changing the sublimation temperature globally is only expected to radially shift the location of the escaping zone without affecting the orientation and opening angle of the outflow.

### 5.2.2. Outflow rate

As the outflows can generally cause the disk to lose mass which affects the accretion process, so the assumption of the stationary disk with a radially constant accretion rate may not be correct. On the other hand, possibly much more material flows out than

finally accretes onto the central black hole, as not only the kinetic luminosity is recently reported to be exceeding the bolometric luminosity of the quasar ([Choi et al. 2020](#)), but also estimations of the outflowing mass in few sources confirm it ([Borguet et al. 2013](#); [Chamberlain et al. 2015](#)). There can be two scenarios to explain this issue: one based on assuming the outflowing material is supplied from somewhere else than the disk itself, while in the second scenario the outflow originates from the disk but the accretion rate must be much higher at large radii ([Naddaf et al. 2022](#)). Some estimates of the outflow within the frame of the 2.5-D FRADO model were made in [Müller et al. \(2022\)](#), but they strongly depend on the additional assumptions since the model directly predicts velocity but not the density of the wind/no of clouds per unit time. This effect is neglected in the current model.

### 5.2.3. Line driving

Our model is based on the outflow launching based on radiation pressure acting on dust. Previous papers predicting the conical outflow were based on line-driving mechanisms.

Formation of a fast funnel-shaped outflow of material from an accretion disk triggered by the disk radiation pressure is reported in many studies in hydro and non-hydro contexts (see e.g. [Proga & Kallman 2004](#); [Risaliti & Elvis 2010](#); [Nomura et al. 2020](#), and the references therein). The models are based on the line-driving mechanism which is appropriate for the highly-ionized part of the BLR located at a few hundred gravitational radii,  $r_g$  while the dust-driven outflow is launched at a few thousand  $r_g$ , more appropriate for (partially) dusty outflow observed BAL.

That does not mean that line driving is not important for BAL. Dust-driven outflow reaches only moderate velocities while some measured BAL velocities approach the fraction of the speed of light, and may result from line-locking mechanism (e.g. Foltz et al. 1987; Vilkoviskij & Irwin 2001; Lin & Lu 2020). However, the outflow geometry is set in the first, dust-driven stage, so our approach should be a good approximation for the BAL geometry - the mean inclination of the stream and the covering factor - while detailed modelling of the outflow acceleration at the later stages may require adding the line driving to the model.

### 5.3. Determination of the parameters in the quasar sample

In the present work, we selected only these sources from Shen et al. (2011) which have the mass determination based on Mg II. Nevertheless, even in this case, the mass determination can have a considerable error, and this leads to even large uncertainty in the derivation of the Eddington ratio, as this requires the use of bolometric correction and an assumption that there is no intrinsic extinction of the continuum by dust. This might lead to large errors in some sources. However, statistically, the values of the mass and Eddington rate may not be strongly biased although an improvement in the sample selection could be likely done in the future.

### 5.4. Implications for torus

Measurements of X-ray occultation indicate the presence of highly dynamical X-ray obscuring clouds at all scales from the onset of BLR outwards to the torus (Bianchi et al. 2012; Markowitz et al. 2014; Torricelli-Ciamponi et al. 2014).

Observational studies support the presence of the obscuring torus, with moderate up to very high opening angles (Lawrence & Elvis 2010; Alonso-Herrero et al. 2011; Guainazzi et al. 2016; Prince et al. 2022). However, in excellent agreement with X-ray spectroscopy, the best-fit opening angle of 50 degrees is reported for the clumpy model of torus (Nenkova et al. 2008a,b).

Independent studies report on the expectations for higher metallicity in quasars when the Eddington ratio of the source increases (e.g. Panda et al. 2018, 2019; Śniegowska et al. 2021; Shin et al. 2021; Panda & Skorek 2022; Garnica et al. 2022).

On the other hand, we simulated the motion of clumpy-dusty material lifted from the disk surface forming the BLR and outflowing towards the torus, and the results for the cases with the torus present at moderate opening angles between 45 to 60 showed a better consistency with the observational data if higher metallicities are adopted. This can be considered as a relatively strong hint to the formation of the torus as a posteriori to the BLR.

## 6. Summary

We tested a scenario claiming that the BAL phenomenon in QSOs is not a temporary stage of their life. In this scenario, we see the BAL effect only if the line of sight is within the spatially limited and collimated massive outflow (shallow) cone covering only a fraction of the sky from the point of view of the nucleus. We use the theoretical model - 2.5D FRAVO - which predicts the cone geometry. The model is based on dust driving in the BLR region.

We calculated the probability of observing a BAL QSO defined as the ratio of the solid angle of the outflow over the full

sky, including considerations on the presence/absence of obscuring torus. We compared our results with observational data for a sample of SDSS QSOs consisting of two sub-populations of BAL and non-BAL QSOs. We found that both in the model and in the data the BAL phenomenon mostly happens for sources with black hole masses larger than  $10^8 M_\odot$ , the effect gets stronger with accretion rate, and also high metallicities are more likely in QSOs showing BAL features if the presence of torus is taken into account.

*Acknowledgements.* The project was partially supported by the Polish Funding Agency National Science Centre, project 2017/26/A/ST9/00756 (MAESTRO 9), and MNiSW grant DIR/WK/2018/12. M. L. M.-A. acknowledges financial support from Millennium Nucleus NCN19\_058 (TITANs). S.P. acknowledges the financial support from the Conselho Nacional de Desenvolvimento Científico e Tecnológico (CNPq) Fellowship (164753/2020-6). M.H.N. acknowledges the financial support for this research on the basis of a grant awarded in the 2022 competition for young scientists by the Center for Theoretical Physics, Polish Academy of Sciences.

## References

Allen, J. T., Hewett, P. C., Maddox, N., Richards, G. T., & Belokurov, V. 2011, MNRAS, 410, 860  
 Alonso-Herrero, A., Ramos Almeida, C., Mason, R., et al. 2011, ApJ, 736, 82  
 Baskin, A. & Laor, A. 2018, MNRAS, 474, 1970  
 Bautista, M. A., Dunn, J. P., Arav, N., et al. 2010, ApJ, 713, 25  
 Bianchi, S., Maiolino, R., & Risaliti, G. 2012, Advances in Astronomy, 2012, 782030  
 Borguet, B. C. J., Arav, N., Edmonds, D., Chamberlain, C., & Benn, C. 2013, ApJ, 762, 49  
 Chamberlain, C., Arav, N., & Benn, C. 2015, MNRAS, 450, 1085  
 Choi, H., Leighly, K. M., Dabbieri, C., et al. 2022a, ApJ, 936, 110  
 Choi, H., Leighly, K. M., Terndrup, D. M., et al. 2022b, ApJ, 937, 74  
 Choi, H., Leighly, K. M., Terndrup, D. M., Gallagher, S. C., & Richards, G. T. 2020, ApJ, 891, 53  
 Czerny, B., Du, P., Wang, J.-M., & Karas, V. 2016, ApJ, 832, 15  
 Czerny, B. & Hryniwicz, K. 2011, A&A, 525, L8  
 Czerny, B., Li, Y.-R., Hryniwicz, K., et al. 2017, ApJ, 846, 154  
 Czerny, B., Modzelewska, J., Petrogalli, F., et al. 2015, Advances in Space Research, 55, 1806  
 Di Matteo, T., Springel, V., & Hernquist, L. 2005, Nature, 433, 604  
 Drew, J. E. & Bokkenberg, A. 1984, MNRAS, 211, 813  
 Dunn, J. P., Bautista, M., Arav, N., et al. 2010, ApJ, 709, 611  
 Elvis, M. 2000, ApJ, 545, 63  
 Elvis, M. 2006, Mem. Soc. Astron. Italiana, 77, 573  
 Elvis, M. 2012, in Astronomical Society of the Pacific Conference Series, Vol. 460, AGN Winds in Charleston, ed. G. Chartas, F. Hamann, & K. M. Leighly, 186  
 Foltz, C. B., Weymann, R. J., Morris, S. L., & Turnshek, D. A. 1987, ApJ, 317, 450  
 Garnica, K., Negrete, C. A., Marziani, P., et al. 2022, A&A, 667, A105  
 Gravity Collaboration, Dexter, J., Shangguan, J., et al. 2020, A&A, 635, A92  
 Guainazzi, M., Risaliti, G., Awaki, H., et al. 2016, MNRAS, 460, 1954  
 Hamann, F., Herbst, H., Paris, I., & Capellupo, D. 2019, MNRAS, 483, 1808  
 Hopkins, P. F., Murray, N., & Thompson, T. A. 2009, MNRAS, 398, 303  
 Juarez, Y., Maiolino, R., Mujica, R., et al. 2009, A&A, 494, L25  
 Knigge, C., Scaringi, S., Goad, M. R., & Cottis, C. E. 2008, MNRAS, 386, 1426  
 Korista, K. T., Bautista, M. A., Arav, N., et al. 2008, ApJ, 688, 108  
 Krolik, J. H. 1999, Active Galactic Nuclei. From the Central Black Hole to the Galactic Environment  
 Krolik, J. H. & Voit, G. M. 1998, ApJ, 497, L5  
 Lawrence, A. & Elvis, M. 2010, ApJ, 714, 561  
 Lin, Y.-R. & Lu, W.-J. 2020, MNRAS, 497, 1457  
 Lynds, C. R. 1967, ApJ, 147, 396  
 Markowitz, A. G., Krumpe, M., & Nikutta, R. 2014, MNRAS, 439, 1403  
 Martínez-Aldama, M. L., del Olmo, A., Marziani, P., et al. 2018, A&A, 618, A179  
 Mathis, J. S., Rumpl, W., & Nordsieck, K. H. 1977, ApJ, 217, 425  
 Matsuoka, K., Nagao, T., Marconi, A., Maiolino, R., & Taniguchi, Y. 2011, A&A, 527, A100  
 Mejía-Restrepo, J. E., Trakhtenbrot, B., Lira, P., Netzer, H., & Capellupo, D. M. 2016, MNRAS, 460, 187  
 Moe, M., Arav, N., Bautista, M. A., & Korista, K. T. 2009, ApJ, 706, 525  
 Müller, A. L., Naddaf, M.-H., Zajaček, M., et al. 2022, ApJ, 931, 39  
 Murray, N., Chiang, J., Grossman, S. A., & Voit, G. M. 1995, ApJ, 451, 498

Naddaf, M. H. & Czerny, B. 2022, A&A, 663, A77

Naddaf, M.-H., Czerny, B., & Szczerba, R. 2020, *Frontiers in Astronomy and Space Sciences*, 7, 15

Naddaf, M.-H., Czerny, B., & Szczerba, R. 2021, ApJ, 920, 30

Naddaf, M.-H., Czerny, B., & Zajaček, M. 2022, *Dynamics*, 2, 295

Nenkova, M., Sirocky, M. M., Ivezić, Ž., & Elitzur, M. 2008a, ApJ, 685, 147

Nenkova, M., Sirocky, M. M., Nikutta, R., Ivezić, Ž., & Elitzur, M. 2008b, ApJ, 685, 160

Nomura, M., Ohsuga, K., & Done, C. 2020, MNRAS, 494, 3616

Panda, S., Czerny, B., Adhikari, T. P., et al. 2018, ApJ, 866, 115

Panda, S., Martínez-Aldama, M. L., Marinello, M., et al. 2020, ApJ, 902, 76

Panda, S., Marziani, P., & Czerny, B. 2019, ApJ, 882, 79

Panda, S. & Skorek, E. J. 2022, in XL Polish Astronomical Society Meeting, ed. E. Szuszkiewicz, A. Majczyna, K. Małek, M. Ratajczak, E. Niemczura, U. Bąk-Stęślicka, R. Poleski, M. Bilicki, & Ł. Wyrzykowski, Vol. 12, 72–75

Prince, R., Hryniewicz, K., Panda, S., Czerny, B., & Pollo, A. 2022, ApJ, 925, 215

Proga, D. & Kallman, T. R. 2004, ApJ, 616, 688

Risaliti, G., Bianchi, S., Matt, G., et al. 2005, ApJ, 630, L129

Risaliti, G. & Elvis, M. 2010, A&A, 516, A89

Rodríguez Hidalgo, P. & Rankine, A. L. 2022, ApJ, 939, L24

Röllig, M., Szczerba, R., Ossenkopf, V., & Glück, C. 2013, A&A, 549, A85

Shen, Y., Richards, G. T., Strauss, M. A., et al. 2011, ApJs, 194, 45

Shen, Y., Wu, J., Jiang, L., et al. 2019, ApJ, 873, 35

Shin, J., Woo, J.-H., Nagao, T., Kim, M., & Bahk, H. 2021, ApJ, 917, 107

Śniegowska, M., Marziani, P., Czerny, B., et al. 2021, ApJ, 910, 115

Sulentic, J. W., Dultzin-Hacyan, D., Marziani, P., et al. 2006, *Revista Mexicana de Astronomía y Astrofísica*, 42, 23

Surdej, J. & Swings, J. P. 1981, A&A, 96, 242

Tolea, A., Krolik, J. H., & Tsvetanov, Z. 2002, ApJ, 578, L31

Torricelli-Ciamponi, G., Pietrini, P., Risaliti, G., & Salvati, M. 2014, MNRAS, 442, 2116

Turnshek, D. A. 1988, in *QSO Absorption Lines: Probing the Universe*, ed. J. C. Blades, D. A. Turnshek, & C. A. Norman, 17

Vestergaard, M. 2003, ApJ, 599, 116

Vestergaard, M. & Peterson, B. M. 2006, ApJ, 641, 689

Vilkoviskij, E. Y. & Irwin, M. J. 2001, MNRAS, 321, 4

Voit, G. M., Weymann, R. J., & Korista, K. T. 1993, ApJ, 413, 95

Waters, T., Proga, D., & Dannen, R. 2021, arXiv e-prints, arXiv:2101.09273

Weymann, R. J., Morris, S. L., Foltz, C. B., & Hewett, P. C. 1991, ApJ, 373, 23

Young, S., Corbett, E. A., Giannuzzo, M. E., et al. 1999, MNRAS, 303, 227